

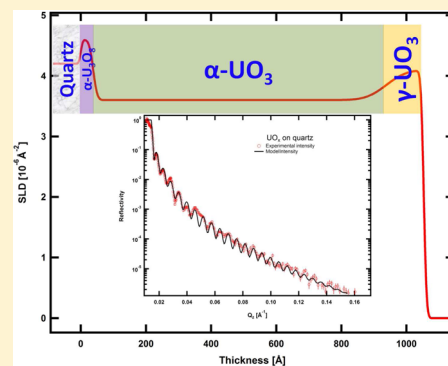
1 Characterization of Chemical Speciation in Ultrathin Uranium Oxide 2 Layered Films

3 Heming He,[†] P. Wang,[‡] D. D. Allred,[§] Jaroslaw Majewski,[‡] M. P. Wilkerson,[†] and Kirk D. Rector^{*†}

4 [†]Chemistry Division, and [‡]Lujan Neutron Scattering Center, Los Alamos National Laboratory, Los Alamos, New Mexico 87545,
5 United States

6 [§]Department of Physics and Astronomy, Brigham Young University, Provo, Utah 84602, United States

7 **ABSTRACT:** A unique approach to detect chemical speciation and distribution
8 on nanometer-scale nuclear materials has been achieved by the combination of
9 neutron reflectometry and shell-isolated surface-enhanced Raman spectroscopy.
10 Both surface and underlying layers of the uranium oxide materials were
11 determined with angstrom-level resolution. Our results reveal that the UO_x film
12 is composed of three sublayers: an ~ 38 Å thick layer of U_3O_8 formed along the
13 UO_x /substrate interface; the adjacent sublayer consists of an ~ 900 Å thick single
14 phase of $\alpha\text{-UO}_3$, and the top layer is $\gamma\text{-UO}_3$ with a thickness of ~ 115 Å.



15 **T**he complexity of uranium oxide—arguably the most
16 important technological form of uranium—has been
17 described as “awesome”, exhibiting some of the most intriguing
18 and challenging chemistry known.¹ Indeed, the compositions of
19 uranium oxides are numerically variable,² and the compositions
20 of the various oxides can be affected by environmental
21 conditions. Even the deceptively simple cubic structure of
22 UO_2 masks incredibly complex speciation following exposure to
23 air.^{3,4} The scientific challenge is to identify, measure, and
24 understand those aspects of actinide speciation that carry
25 information about the changes within these materials as a
26 function of aging conditions without disturbing their micro-
27 structures.

28 Conceptually, the presence and distribution of chemical
29 species on or in an ultrathin film, which may be formed during
30 production or reprocessing of nuclear materials, or further
31 reaction following transportation and/or environmental aging
32 from contact with atmosphere resulting in oxidation, hydration,
33 and other reactions, could contain rich forensic information.
34 Characterization of the film and its physical and chemical
35 signatures could provide unprecedented ability to assess or
36 interpret characteristics that related to provenance, age, and fate
37 of the material.

38 However, a critical component for limiting the ability to
39 access those chemical intelligence signatures is that many
40 current methods are effective for bulk analyses of homogenized
41 samples and therefore yield sample average properties.
42 Therefore, revolutionary approaches to acquire spatially and,
43 more importantly, depth-resolved quantitative and nondestructive
44 chemical and physical signatures to the nanometer-scale
45 could have direct benefit to the future of nuclear forensic
46 science.

47 Here, we demonstrate for the first time, the direct usage of
48 two powerful techniques, neutron reflectometry (NR)^{5–7} and
49 surface-enhanced Raman spectroscopy (SERS),⁸ to non-
50 destructively characterize the chemical speciation in an ultrathin
51 uranium oxide film with angstrom-level spatial resolution along
52 the direction perpendicular to the substrate while applying NR
53 technology. Using a $^{238}\text{UO}_x$ thin-film sample prepared using
54 reactive physical vapor deposition onto a quartz substrate, the
55 analyses reveal that the 1053 Å thick film is composed of three
56 layers of varying thickness and phases. The measurements
57 establish the ability to determine the chemical speciation and
58 depth of both the surface and underlying layers of a film that
59 could lead to a quantitative measure of oxidation kinetics in
60 these and other materials. This fundamental approach provides
61 the ability to characterize the rates of changes in environmental
62 samples. The practical implication of this behavior is the ability
63 to maintain stable forms of nuclear fuel over time, to provide
64 safe mechanisms for storage of spent nuclear fuel, to predict
65 transport and fate, and to assess the chemical history of actinide
66 materials for forensic analyses.

67 ■ METHODS SUMMARY

68 **Preparation of Uranium Oxide Thin Films.** The uranium
69 oxide thin film was deposited by reactive dc magnetron
70 sputtering using an argon/oxygen mixture as the working gas
71 under moderate vacuum condition with a base pressure less
72 than 2×10^{-4} Torr. In such a system, a magnet is placed
73 beneath the uranium metal targets to contain the plasma, argon,

Received: September 7, 2012

Accepted: November 6, 2012

74 or oxygen in our case (which was produced by applying a dc
75 voltage to ionize the Ar/O₂ mixture), to the region directly
76 above the targets. This allows the plasma to hit the negatively
77 charged targets (typical voltage of ~400 V) knocking off
78 uranium atoms that will be readily oxidize by O₂/Ar mixture
79 and then deposit on the substrate above. Since the thickness,
80 uniformity, and the smoothness of the thin film are essential for
81 NR measurements, efforts were made to even out cross
82 substrate thickness variations: A longer substrate–target
83 distance was chosen to promote film thickness uniformity
84 across the substrate, and more importantly, a multistep reactive
85 deposition was utilized to minimize the preferential film growth
86 that can adversely affect film quality. During the reactive
87 deposition process, the substrate was rotated to even out source
88 distribution anomalies and the sample tray was also slowly
89 rotated over the targets to deposit a smooth film with desired
90 uniformity and thicknesses. By controlling the partial pressures
91 of Ar and O₂ (typically, the argon pressure was about 4 × 10⁻³
92 Torr and the oxygen pressure was 2 × 10⁻⁴ Torr) entering into
93 the sputtering system, the composition of the uranium oxide
94 formed may be controlled.

95 **Neutron Reflectometry Measurements.** Neutron reflectometry
96 experiments were performed on the surface profile
97 analysis reflectometer (SPEAR), a time-of-flight reflectometer
98 at the Los Alamos National Laboratory Lujan Neutron
99 Scattering Center.⁷ Unlike the X-ray photons (the ability of
100 an atom to scatter X-rays is proportional to its electron
101 density), neutrons interact with the nucleus via short-range
102 nuclear forces. The ratio of slow neutron coherent scattering
103 amplitudes of uranium and oxygen is 1.47⁹ (for X-rays the
104 scattering amplitude of oxygen is much smaller than that of
105 uranium), so that an appreciable proportion of the scattered
106 intensity come from oxygen, offering the possibility to
107 distinguish between the complex uranium oxide family. More
108 importantly, the NR technique is feasible to investigate systems
109 which are laterally uniform in the range of coherency of the
110 neutron beam (usually several tens of square micrometers),
111 with total thickness less than 5000 Å and with rms roughness
112 less than 100 Å. During an NR experiment, neutrons impinge
113 on a sample at a small angle, θ , and the ratio R of elastically and
114 specularly scattered/incident neutrons was measured as a
115 function of the neutron momentum transfer vector:

$$116 \quad Q_z = \frac{4\pi \sin(\theta)}{\lambda} \quad (1)$$

117 where λ is the neutron wavelength. Neutrons are reflected by
118 the interfaces within the system and interfere creating series of
119 characteristic oscillatory modulation of the reflected intensity, a
120 pattern known as Kiessig fringes. In general, the spacing of the
121 fringes, ΔQ_z , carries information about thicknesses, t , within the
122 thin film. For a monolayered structure, the thickness of the film
123 is related to the fringe spacing by

$$124 \quad t = \frac{2\pi}{\Delta Q_z} \quad (2)$$

125 while the amplitude of the Kiessig fringes depends on the
126 neutron scattering length density (SLD) contrast and roughness
127 of the system. Fitting the specular reflectometry data
128 provides information regarding the depth profile of coherent
129 SLD distribution perpendicular to the sample surface, here
130 designated the z -direction, with angstrom precision. It is
131 important to note that the SLD, which is the product of the

number density of atoms and their nuclear coherent scattering
132 lengths, is a value unique to a particular chemical composition
133 and specific structure of the measured film and can be
134 considered as the fingerprint to identify the materials. The SLD
135 calculation tool developed by NIST (available online at <http://www.ncnr.nist.gov/resources/sldcalc.html>) was utilized for the
136 calculation of the SLD value for some common phases in the
137 uranium oxide system, Figure 1. ²³⁸U and ¹⁶O are used for the
138 calculations. 139 f

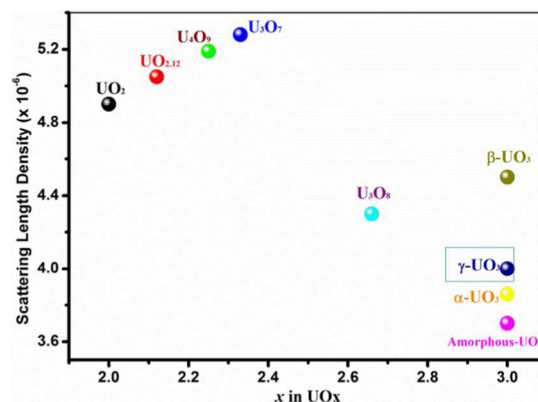


Figure 1. Calculated value of the nuclear scattering length density (SLD) for some common phases in the uranium oxide system. The calculations are based on specific densities published in literature (refs 10 and 11).

Raman Instrumentation. Raman and SERS experiments 141
142 were performed using a Ti:sapphire laser (Mira 900-P, 142
Coherent, Palo Alto, CA) turned to 776 nm. The incident 143
laser was filtered spectrally by a short-pass filter at 785 nm 144
(RazorEdge SP01-785RU-25, Semrock, Rochester, NY). The 145
collimated beam was focused to a line using a plano-convex BK 146
7 150 mm focal length cylindrical lens (CKX150AR.16, 147
Newport Corp., Irvine, CA) and was then redirected to the 148
back of an inverted microscope (Carl Zeiss Axiovert 200, 149
Göttingen, Germany) by a Raman edge dichroic (z785rdc, 150
Chroma Technology, Rockingham, VT). A 63× air objective 151
lens (Carl Zeiss) focused the laser beam to a line approximately 152
1 μm wide and 250 μm long on the sample, with a total power 153
of 90 mW at the sample.^{12,13} Raman images were collected 154
through the same spectrometer with a backscattering 155
configuration on the surface of the sample, which was mounted 156
on an x - y translation microscope stage (MS2000XY stage, 157
Applied Scientific Instrumentation Inc., Eugene, OR) with a 158
submicrometer accuracy and reproducibility. A halogen lamp 159
was used to illuminate the sample for bright-field visualization 160
for sample positioning, then turned off for Raman measure- 161
ments. The inelastic (Raman) light scattering was focused by a 162
150 mm spherical lens onto a 50 μm wide slit at the entrance of 163
a Holospec $f/2.2$ spectrograph (Kaiser Optical Systems, Ann 164
Arbor, MI) and filtered with a Holographic SuperNotch-Plus 165
filter (HSPF-785.0AR-2.0, Kaiser Optical Systems, Ann Arbor, 166
MI). The signal was then dispersed with a holographic grating 167
(HSG-785-LF, Kaiser) and imaged by a liquid nitrogen-cooled 168
CCD camera (LN/CCD-1024E, Princeton Instruments, 169
Trenton, NJ) with spectral information, Raman shift, along 170
the horizontal direction and spatial information along the 171
vertical direction. The spectrometer was calibrated spectrally 172
with 4-acetamidophenol and spatially using lines in the seventh 173
group of a USAF-1951 resolution test target. The spectral 174

175 resolution of the spectrograph ranges from 3 to 5 cm^{-1} across
 176 the Raman data range acquired, and the spatial resolution of the
 177 microscope was approximately 1 μm laterally and 2 μm axially.
 178 Custom-written National Instruments Labview code controls
 179 the CCD array and all of the other aspects of the microscope.
 180 The Raman image was acquired with a total exposure time of
 181 60 s and consists of 256 spectra sampled at regular spatial
 182 intervals 1.0 μm apart along that line. Apart from the CCD bias
 183 voltage, no other background from the sample was removed
 184 from the original Raman image data. Raman microspectra
 185 (RMS) were acquired from the thin-film samples using the
 186 same spectrometer with a same configuration. The spatial
 187 information was electronically integrated to improve signal-to-
 188 noise ratio. Processing of the spectral data included dark
 189 background subtraction, NIST-calibrated spectral flat field
 190 correction, baseline correction using a concave rubber band
 191 correction algorithm, and normalization.

192 **SERS.** Raman spectroscopy provides a unique approach to
 193 probe rich information about the molecular structure of the
 194 sample, and it has shown the potential to rapidly detect
 195 persistent chemical signature of nuclear material origin long
 196 after release.^{3,14–18} However, spontaneous Raman scattering
 197 has been suffering its inherently weak and low efficiency of
 198 inelastic photon scattering by molecules. The extremely small
 199 cross sections, typically $\sim 10^{-30}$ to 10^{-25} cm^2 per molecule,
 200 require a large number of analyte molecules to achieve adequate
 201 conversion rates from excitation laser photons to Raman
 202 photons. Therefore, spontaneous Raman spectroscopy has been
 203 considered a technique for structural analysis, rather than a
 204 method for ultrasensitive trace detection.¹⁹

205 However, a novel phenomenon, known as SERS, discovered
 206 in the 1970s^{20–22} could overcome some of these limitations.
 207 Under favorable circumstance, when electrochemically rough-
 208 ened metal surfaces²⁰ or aggregate films²³ or, more commonly,
 209 colloidal metal nanoparticles²⁴ (NPs, in particular Au or Ag)
 210 and their assemblies⁸ oscillated in the local optical fields leads
 211 to strong electric near-field enhancement, this effect acts as an
 212 amplifier for inelastic (Raman) light scattering processes,
 213 transforms Raman spectroscopy from a structural analytical
 214 tool to a structurally sensitive nanoscale probe.²⁵ Currently, two
 215 mechanisms are generally accepted: surface electromagnetic
 216 (EM) field enhancement and chemical contribution. Among
 217 them, the sensitivity of SERS is dominated by the electro-
 218 magnetic enhancement, a particularly intriguing feature that
 219 depends strongly on the size, shape, and gap distance between
 220 SERS nanoparticles, as well as the frequency and polarization of
 221 the excitation laser.

222 Generally, the gap between the two nanospheres is where the
 223 electromagnetic field gives rise to the strongest enhanced
 224 Raman signals, typically a few orders of magnitude greater than
 225 that achievable with single nanoparticles (i.e., without pairing).
 226 For instance, a theoretical value of the SERS enhancement
 227 factor (EF) for isolated gold nanospheres has been estimated to
 228 be 10^3 – 10^4 .²⁶ On the contrary, it could be 10 orders of
 229 magnitude higher for gold nanoclusters that consist of a
 230 minimum of 5–10 paired nanoparticles.¹⁹ Apparently, in
 231 surface-enhanced spectroscopy (SES) applications such as
 232 SERS, it is of critical importance to make intimately paired
 233 nanoparticle clusters and maintain nanometer interparticle
 234 distance. However, too narrow gaps may enable electron
 235 transfer between the two adjacent nanostructures, and once
 236 conductive overlap is established, the field enhancements are

reduced and the energy of gap plasmons can be strongly shifted
 compared with the situation with no conductive overlap.²⁷

The approach using “shell-isolated nanoparticle-enhanced
 Raman spectroscopy” (detailed information of the preparation
 of the shell-isolated Au NPs has been published elsewhere⁸)
 based system known as SHINERS²⁸ has taken advantages of
 the large electromagnetic field enhancements that can be
 generated between adjacent metal regions separated by a
 dielectric shell (i.e., SiO_2) of ~ 2 nm, Figure 2a. The dielectric

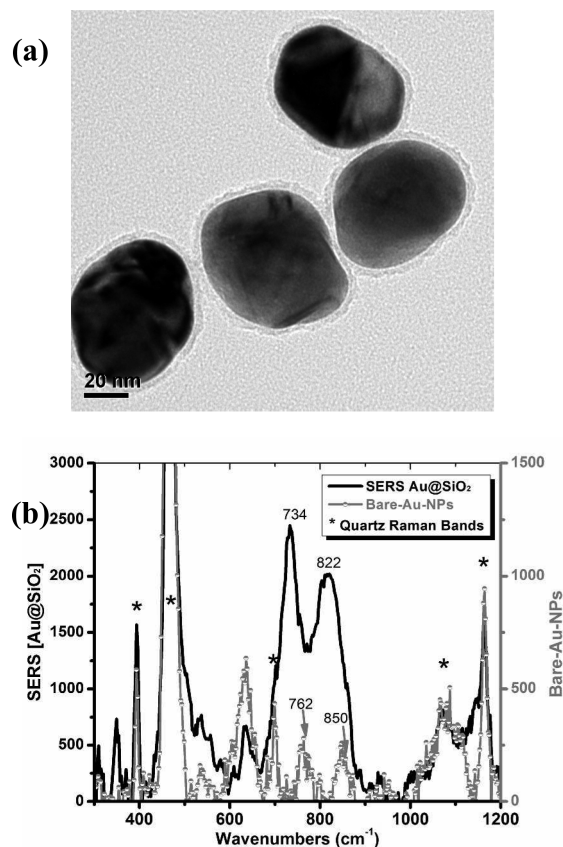


Figure 2. (a) High-resolution transmission electron microscopy image of core–shelled gold nanoparticles ($\text{Au}@\text{SiO}_2$) with an approximate 2 nm dielectric shell, courtesy of Dr. Zhong Qun Tian (Xiamen University). (b) SERS spectra on the UO_3 @quartz sample obtained using bare gold nanoparticles (gray) and SHINERS particles (black).

silica layer acts as a protective coating to prevent unwanted
 nonspecific interaction of the gold with other species, as well as
 to maintain a narrow nanogap between the gold particles and
 avoid a direct contact between them. Apparently, it also allows
 adsorption of the target analyte to be close enough to the gold
 core to experience electromagnetic enhancement and hence an
 increase in the Raman scattering.

A comparison of the SERS spectra on UO_3 @quartz thin film
 obtained using bare gold and shell-isolated gold NPs is shown
 in Figure 2b. The practice of using bare gold NPs as SERS
 particles can be challenging. The spectrum, obtained by using
 50 nm bare gold, present in Figure 2b shows weak SERS effects
 over hundreds of spectra. The weak peaks, center around 763
 and 845 cm^{-1} corresponding to the two Raman active bands of
 A_{1g} and E_g , are expected at 768 and 846 cm^{-1} in spontaneous
 Raman spectrum for bulk γ - UO_3 .

262 Recently, a quantitative measurement of the distribution of
 263 site enhancement in SERS was reported. The hottest SERS-
 264 active sites accounted for only 63 sites in 1 million of the total
 265 sites.²⁹ However, the advantage of using Au@SiO₂ shell-
 266 isolated NPs is that, instead of searching for isolated hot spots
 267 or nanogaps in random nanoparticle aggregates, all of the
 268 individual Au@SiO₂ NPs, distributed like a monolayer,
 269 simultaneously brings thousands of light shiners to the
 270 substrate surface and enhanced Raman signal contributed by
 271 all of them resulting in uniform localized surface plasmons
 272 rather than in sporadic hot spots with an enhancement factors
 273 as high as 10⁷.

274 ■ RESULTS AND DISCUSSION

275 **Neutron Reflectometry Results.** The NR data was
 276 collected from a thin film deposited on monocrystalline α -
 277 quartz substrates by reactive sputtering of a depleted uranium
 278 (99.6% ²³⁸U) metal target (see the Methods Summary section
 279 for details). Specular NR provides detailed information about
 280 the SLD distribution perpendicular to the sample surface. SLD
 281 is used to describe the power of a material to scatter neutrons;
 282 SLD can be calculated according the following equation:

$$283 \text{SLD}_{\text{neutron}} = \rho \frac{N_A}{M} \sum_{i=1}^{\text{atoms}} b_i \quad (3)$$

284 where b_i is the coherent scattering length of the i th atom, ρ is
 285 density, M is molecular mass, and N_A is Avogadro's number.
 286 The SLD value is a unique parameter for a material and is
 287 determined by its chemical composition and mass density.
 288 Moreover, the SLD profile provides information about the
 289 density, thickness, roughness, chemical composition, and hence
 290 possibly the chemical speciation information of thin-film
 291 materials.

292 Figure 3 shows the NR data (circles), the best-fit trace (black
 293 line), and the corresponding SLD profile for the UO_x sample.
 294 The uncertainties of the fitting parameters are listed in Table 1.
 295 The best fit refers to simplest real-space model with meaningful
 296 physical and chemical parameters providing lowest χ^2 value in
 297 the least-squares refinement. In order to determine the SLD
 298 profile of the UO_x film, the dynamical Parratt formalism was
 299 utilized to fit the NR spectrum.³⁰ The literature SLD value of
 300 the quartz substrate and the calculated SLD values (Figure 1 for
 301 details) of up to eight phases have been used as initial values for
 302 the modeling. UO₂, UO_{2+x}, U₄O₉, U₃O₇, α -UO₃, β -UO₃, and γ -
 303 UO₃ were considered as possible phases that are stable under
 304 the experimental conditions. The best fit could be achieved by
 305 using the fitting parameters summarized in Table 1.
 306 Accordingly, the UO_x film is composed of three sublayers
 307 with a total thickness of ~ 1053 Å. Figure 3b schematically
 308 illustrates the real-space best-fit SLD profile of the film in cross
 309 section. In detail, the SLDs of the substrate/film and the film/
 310 air interfaces are 4.6×10^{-6} and 4.1×10^{-6} Å⁻², respectively,
 311 while the SLD of the interior of the film is 3.6×10^{-6} Å⁻².

312 On the basis of these layers' SLD values, it is probable that
 313 the chemical speciation of the UO_x film is mainly UO₃
 314 (excluding the bottom layer) and consists of different phases.
 315 The crystal structure of UO₃ is abnormally deficient within the
 316 entire uranium oxide family. UO₃-related phases have less
 317 dense structures with SLD values varying from 3×10^{-6} to
 318 slightly greater than 4×10^{-6} Å⁻². For instance, there have been
 319 three experimental determinations of the density of α -UO₃:
 320 7.04 g·cm⁻³ (Hoekstra and Siegel¹⁰), 7.25 g·cm⁻³ (Loopstra and

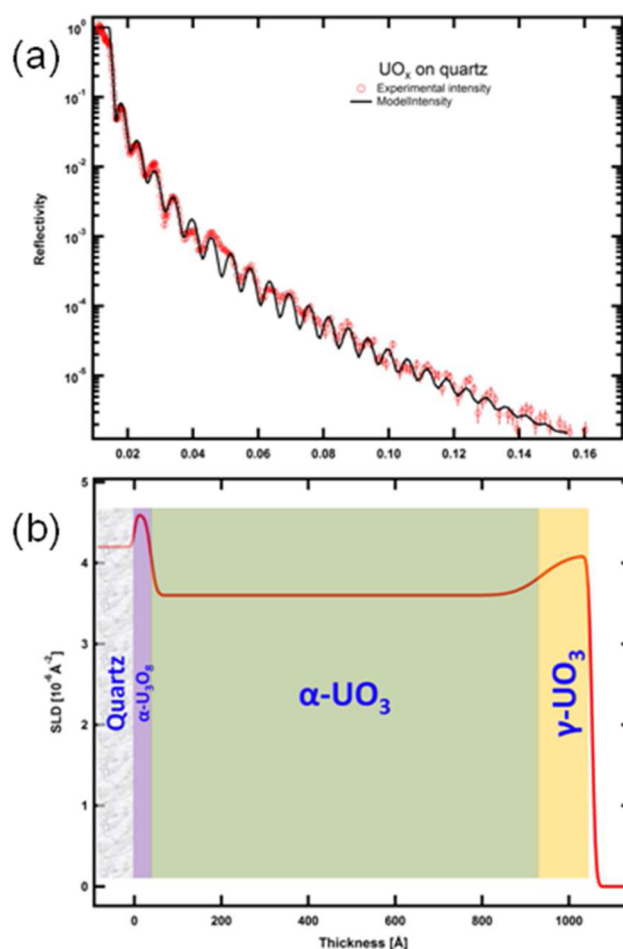


Figure 3. (a) NR spectrum in the form of R vs Q_z from UO_x-coated monocrystalline α -quartz. The data is represented by open circles. The solid lines through the data points are the best fit. (b) Visual representation of the fitting results corresponding to the SLD profiles.

Table 1. Model Parameters Used to Fit NR Data

layer (from substrate)	substrate	layer 1	layer 2	layer 3
thickness (Å) (± 5 Å)	infinite	38	900	115
SLD (10^{-6} Å ⁻²) (± 0.1 Å ⁻²)	4.2	4.6	3.6	4.1
roughness (Å) (± 2 Å)	5	10	50	7
assignment	quartz	U ₃ O ₈	α -UO ₃	γ -UO ₃

321 Cordfunke¹¹), and 7.30 g·cm⁻³ (Siegel and Hoekstra³¹). All of
 322 them are lower than the value of 8.46 g·cm⁻³ calculated using
 323 the unit-cell parameters,³² which implies a vacancy concen-
 324 tration of $\sim 14\%$, if the densities of Loopstra and Cordfunke
 325 and Siegel and Hoekstra are used, or 17% based on the earlier
 326 Hoekstra and Siegel determination.

327 It is likely that the sublayer of substrate/UO_x film interface
 328 (layer 1), which shows highest SLD value, is due to the
 329 heteroepitaxial growth of U₃O₈ as suggested by the SLD
 330 value from NR measurements and the band gap value
 331 determined from spectroscopic ellipsometry measurements
 332 and density functional theory (DFT) calculations.³³ U₃O₈ is
 333 stable in an orthorhombic form, α -U₃O₈, at ambient conditions
 334 and transforms to a trigonal modification at ~ 400 °C.³⁴

335 In contrast, the adjacent sublayer (layer 2) has the lowest
 336 SLD value and can be considered as the bulk film. It consists of
 337 an ~ 900 Å thick single phase of uranium oxide with a constant

338 SLD value, which could be assigned to α - UO_3 . α - UO_3 is stable
 339 under ambient conditions and is generally regarded as a
 340 uranium-deficient form of α - U_3O_8 . It has an unusual structure
 341 with a large concentration of disordered cation vacancies and
 342 ordered anion vacancies.³² This assignment has been confirmed
 343 by X-ray diffraction (XRD) measurement indicating the
 344 presence of hexagonal α - UO_3 (Figure 4). Additionally, α -

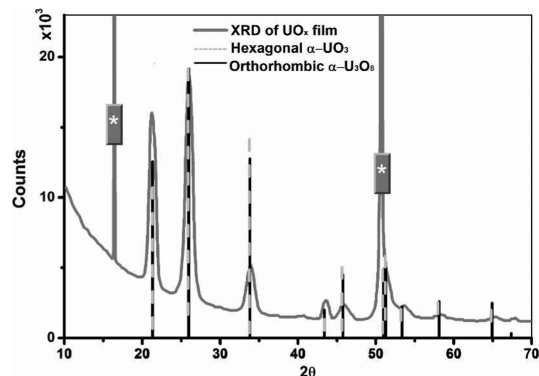


Figure 4. Continuous gray curve shows the XRD pattern (Cu, $K\alpha$) recorded on the UO_x thin film deposited on a monocrystalline quartz substrate indicating the existence of a hexagonal structure of α - UO_3 . The vertical gray (dashed) lines indicate the calculated positions of the Bragg diffraction peaks for hexagonal α - UO_3 phase [adopted from the PDF database (www.icdd.com)], whereas the solid black vertical bars represents closely related orthorhombic structure α - U_3O_8 . [The asterisks indicate the two strong peaks originated from the substrate (2θ around 16 and 51).]

345 U_3O_8 (black traces) and α - UO_3 (dashed gray traces) are
 346 structurally closely related³⁴ with almost identical XRD
 347 patterns, only differing in relative intensities in Figure 4.

However, the preferential growth of α - U_3O_8 appears to be
 348 more favorable than that of α - UO_3 along the substrate interface.
 349 Previous reports show that pinning the crystal lattice in epitaxial
 350 films to form a denser than normal and single-crystal-like thin
 351 layer of oxides is possible. It is hypothesized that a similar
 352 mechanism is active for the uranium oxides on monocrystal
 353 quartz (α -quartz) as well. Even if this is the case, the α - U_3O_8
 354 lattice does not perfectly match the microstructure of α -quartz.
 355 It is well-known that α -quartz crystallizes in the trigonal crystal
 356 system, space group $P3_121$ or $P3_221$.³⁵ Consequently, this
 357 heteroepitaxy effect effectively extends from the interface of the
 358 α -quartz substrate beyond a thickness of several monolayers of
 359 α - U_3O_8 , ~ 38 Å. The top, atmosphere-exposed, layer (layer 3)
 360 with an SLD value up to $\sim 4.1 \times 10^{-6} \text{ \AA}^{-2}$ can be assigned to γ -
 361 UO_3 . Despite the fact that seven different phases can exist in
 362 the UO_3 system, γ - UO_3 is thermodynamically the most stable
 363 phase and has a theoretical SLD value slightly in excess of $4 \times$
 364 10^{-6} \AA^{-2} (Figure 1).
 365

Surface-Enhanced Raman Spectroscopy Result. In
 366 order to verify the NR results, a series of investigations were
 367 conducted on the same uranium oxide film using spontaneous
 368 Raman and SERS techniques. Scanning electron microscopy
 369 (SEM) imagery, presented in Figure 5a, indicate nearly pristine
 370 films on the tens of nanometers distance scale. The Raman
 371 responses versus spatial locations of this type of location were
 372 mapped on the uranium oxide film (Figure 5b). The
 373 spontaneous Raman image measured an intense and narrow
 374 band centered at $\sim 465 \text{ cm}^{-1}$ that corresponds to the A_1
 375 vibrational mode of α -quartz.³⁶ There was no noticeable
 376 Raman response associated with the uranium oxide film,
 377 presumably due to the minute amount of material present being
 378 below the detection limit of the microscope.^{12,13} In contrast,
 379 the SERS approach, based on system known as SHINERS,⁸ 380

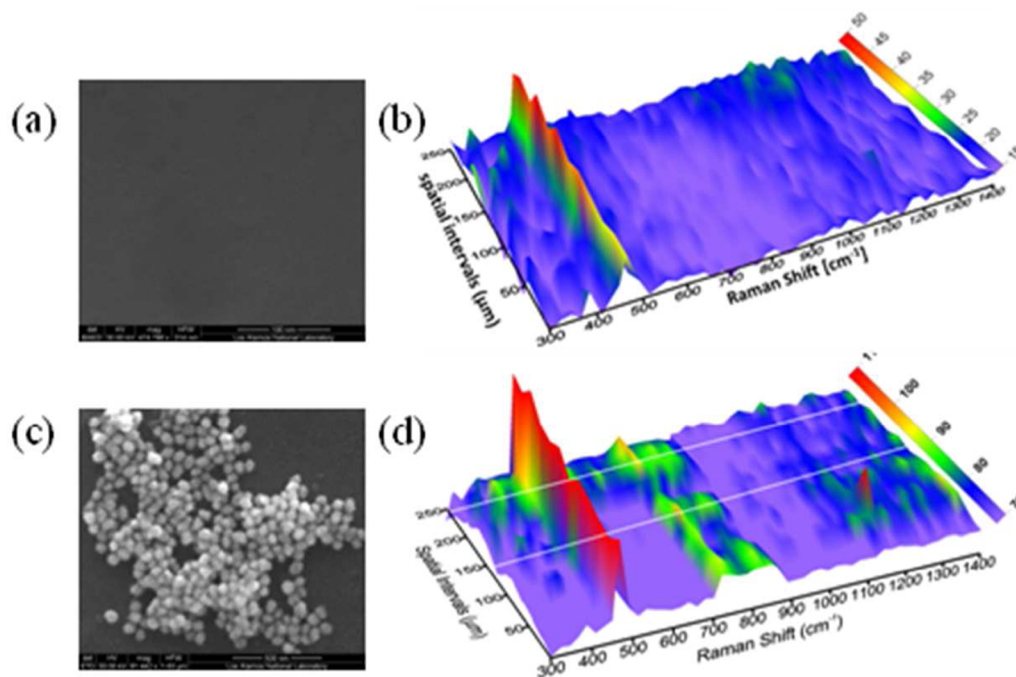


Figure 5. (a) SEM micrograph showing morphological features of an ~ 100 nm UO_x thin film grown on a monocrystalline α -quartz substrate and (b) its space–wavelength Raman images. (c) SEM image of SiO_2 -shell-isolated Au NPs deposited on the UO_x thin film. (d) The corresponding space–wavelength SERS image. Space–wavelength Raman (or SERS) images were obtained in a wavelength range from 100 to 2000 cm^{-1} at up to 256 linear locations (pixels) with an integration time of 60 s.

381 uses ~ 50 nm Au-core NPs with an ~ 2 nm protective silica
 382 (SiO_2) shell coating (Figure 2a). These SERS NPs were drop-
 383 cast onto the surface of the uranium oxide thin film, the water
 384 was allowed to evaporate, and they were imaged with SEM
 385 (Figure 5c). The resulting SERS signatures (Figure 5d) always
 386 demonstrate broad and intense bands primarily located in the
 387 $630\text{--}850\text{ cm}^{-1}$ range and often demonstrated bands in the
 388 $200\text{--}420\text{ cm}^{-1}$ range. For example, a cross section of Figure 5d
 389 taken at $y \sim 140\ \mu\text{m}$ is an example of the former condition,
 390 while a cross section taken at $y \sim 240\ \mu\text{m}$ is an example of the
 391 latter. Lines were added at these positions in Figure 5d to guide
 392 the eye.

393 To study this effect more closely, the SERS spectra (Figure
 394 6a) were collected from an optically pristine appearing portion

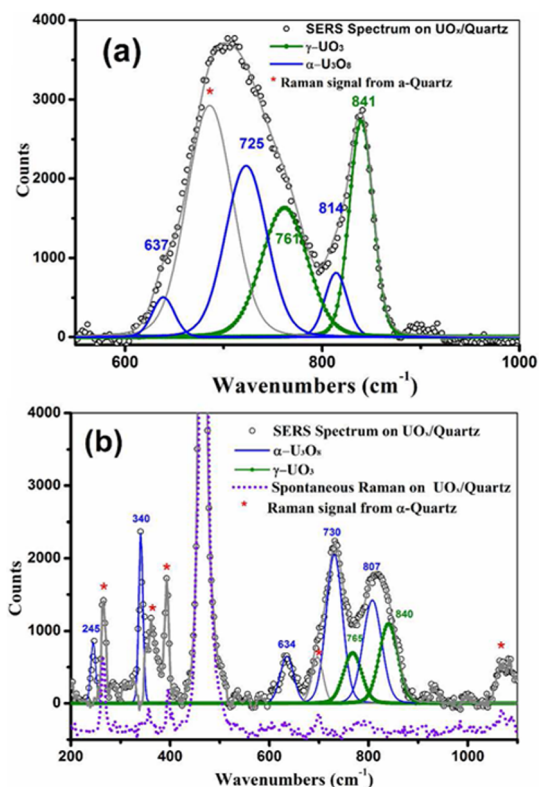


Figure 6. (a) Representative SERS spectrum obtained on an optically pristine appearing portion of the UO_x thin film showing strong $\gamma\text{-UO}_3$ and weak $\alpha\text{-U}_3\text{O}_8$ signatures. (b) Representative SERS spectrum recorded on an optically damaged appearing location of the thin film showing significant relative increase in the $\alpha\text{-U}_3\text{O}_8$ signatures compared to $\gamma\text{-UO}_3$. Spontaneous Raman signatures from the substrate are marked with asterisks.

395 of the film showing complicated features in the region of 600--
 396 900 cm^{-1} . These bands can be deconvolved into the bands
 397 centered at ~ 725 , ~ 760 , ~ 815 , and $\sim 841\text{ cm}^{-1}$. Accordingly,
 398 the SERS results suggest that the chemical speciation of the
 399 UO_3 film is composed of at least two different phases, and the
 400 dominant phase presented on the top surface layer is $\gamma\text{-UO}_3$ in
 401 nature. In $\gamma\text{-UO}_3$, uranium is octahedrally coordinated, but it is
 402 distorted by two longer U–O bonds. The structure of $\gamma\text{-UO}_3$
 403 belongs to the D_{3d} space group, and the following lattice
 404 vibrations would be expected:

$$405 \quad [A_{1g}(\text{R}) + 2A_{2u}(\text{IR}) + E_g(\text{R}) + 2E_u(\text{IR})] \quad (4)$$

The two Raman-active bands are expected at 768 and 846 cm^{-1}
 406 in the spontaneous Raman spectrum for bulk $\gamma\text{-UO}_3$.³⁷
 407 However, in the SERS spectra, both bands shift to lower
 408 frequency by ~ 8 and $\sim 5\text{ cm}^{-1}$, respectively. This red shift may
 409 be attributed to the errors of deconvolving the weak and broad
 410 peaks, or the confinement of phonons in the nanomaterials,³⁸
 411 or both. 412

Additionally, the other two bands ~ 725 and $\sim 815\text{ cm}^{-1}$ do
 413 not match any uranium trioxide compounds, but band positions
 414 are in close agreement with two of its most intense Raman
 415 bands of $\alpha\text{-U}_3\text{O}_8$.³⁹ The SERS effect is inherently a short-
 416 distance effect, and detection through the thick $\alpha\text{-UO}_3$ layer is
 417 improbable. However, scratching damage could create some
 418 defect sites for the particles to deposit into and therefore detect
 419 lower layers. This hypothesis is supported from the SERS
 420 measurements that were performed on the locations that
 421 appeared optically to be damaged, Figure 6b. The SERS spectra
 422 obtained on locations where top surface layers were partially
 423 removed shows a relatively stronger contribution from those
 424 two bands than those spectra acquired from the top layer of $\gamma\text{-}$
 425 UO_3 in pristine regions. Additional bands, Figure 6b, were
 426 observed at 245 , 347 , and $\sim 633\text{ cm}^{-1}$, etc. These new bands
 427 taken altogether with more intense ~ 725 and $\sim 815\text{ cm}^{-1}$ bands
 428 further confirm the existence of $\alpha\text{-U}_3\text{O}_8$ in the underlying layers
 429 of the thin film.⁴⁰ 430

The most commonly accepted structure model for $\alpha\text{-U}_3\text{O}_8$
 431 consists of a pentagonal bipyramid⁴¹ in which the structure is
 432 simply regarded as three embedded noninteracting uranium
 433 oxide units: UO_2 and hexagonal UO_3 with a ratio of 1:2.⁴²
 434 Indeed it is not necessarily true; in reality, the Raman spectrum
 435 of $\alpha\text{-U}_3\text{O}_8$ is somewhat more complex, especially at lower
 436 frequencies. Obviously, the higher frequency bands at ~ 730
 437 and $\sim 810\text{ cm}^{-1}$ in the SERS spectrum are associated with the
 438 embedded octahedral UO_3 unit in U_3O_8 , but they are red-
 439 shifted by $\sim 35\text{ cm}^{-1}$ compared to pure $\gamma\text{-UO}_3$. These red shifts
 440 are consistent with the spontaneous Raman results obtained on
 441 bulk U_3O_8 samples.³⁷ The bands in the region of $412\text{--}483$
 442 cm^{-1} , which could be associated with the embedded UO_2 unit,
 443 are obscured by the strong Raman responses from the substrate
 444 quartz. Note that previous reports indicate no SERS signal
 445 arises from the SiO_2 coating on the particles themselves.⁸ 446

In general, it is difficult to use SERS to probe atomically flat
 447 single-crystal-like thin-film surfaces, since the surface electro-
 448 magnetic field that gives rise to the SERS signal is greatly
 449 concentrated in the nanogap between at least two intimately
 450 paired nanoparticles (nanoparticles coupling)⁴³ with the analyte
 451 adsorbed in this region. The thin-film form of the analyte
 452 cannot be effectively adsorbed into the gap of the paired
 453 nanoparticles; consequently, the effect of nanoparticles
 454 coupling to produce a strong surface plasmon resonance
 455 would not be expected. As a consequence, this widely pursued
 456 technique has not been commonly employed to study thin-film
 457 surfaces.⁸ Only few studies have been published on this subject
 458 since the discovery of SERS in the mid-1970s,^{20–22} and almost
 459 all of them were limited to tip-enhanced Raman spectroscopy
 460 (TERS) on Au(111) surfaces. The SERS results presented here
 461 show the potential of rapidly detecting the chemical signatures
 462 on a few nanometers (e.g., $4\text{--}10\text{ nm}$ in this study) ultrathin
 463 sublayer of the uranium oxide film. To the best of our
 464 knowledge, this is the first demonstration of the direct use of
 465 SERS on solid nononuclear materials. 466

The results reveal that the UO_x film is composed of three
 467 sublayers: (1) The growth of $\alpha\text{-U}_3\text{O}_8$ along the substrate 468

469 interface is stabilized by pinning the crystal lattice into the
470 substrate lattice to form a denser epitaxial film. (2) This
471 heteroepitaxy effect attenuates rapidly with distance in excess of
472 a several monolayers of UO_x due to the not perfect match in
473 their microstructures between the $\alpha\text{-U}_3\text{O}_8$ and the substrate;
474 consequently, the formation of $\alpha\text{-UO}_3$ (a uranium-deficient
475 form of $\alpha\text{-U}_3\text{O}_8$ with a large concentration of vacancies) is
476 more favorable. (3) Finally, the top, atmosphere-exposed layer
477 will transform to thermodynamically most stable phase of $\gamma\text{-UO}_3$.
478 UO_3 .

479 ■ CONCLUSIONS

480 A unique approach to detect chemical speciation and species
481 distribution on nanoscale nuclear materials has been achieved
482 by the combination of NR and shell-isolated SERS. Using this
483 combination, it is demonstrated, for the first time, the capability
484 of the determination of the chemical speciation signatures on a
485 complex uranium oxide family, namely, both the surface and
486 underlying layers of the nuclear materials with angstrom-level
487 resolution. This capacity is neither achievable using XRD nor
488 Raman spectroscopy since the former is not capable to
489 distinguish between U_3O_8 and $\alpha\text{-UO}_3$ especially in the
490 nanometer scale, while the later is incapable to detect $\alpha\text{-UO}_3$
491 due to the fact that $\alpha\text{-UO}_3$ has no observable Raman signatures.
492 Moreover, the angstrom-resolution measurement of the
493 chemical speciation and their spatial distribution for nuclear
494 materials of technological importance could foster a revolution
495 in our understanding of their oxidative behavior by providing
496 new capabilities to exploit rich forensic or chemical intelligence
497 information and extend fundamental knowledge to assess or
498 interpret the signatures, while leaving the opportunity to
499 employ additional, possibly destructive methods of analysis.
500 While this report is on a sample quite large, the possibility exists
501 to confine the neutron beam to be on the similar scale as
502 commercial X-ray fluorescence microscopes and other
503 techniques currently being applied in the forensics field. The
504 development of this method may also be applicable to a broad
505 range of scientific disciplines such as environmental transport
506 and fate, stockpile stewardship, nuclear fuels, nonproliferation,
507 forensic science, and development of actinide standards.

508 ■ AUTHOR INFORMATION

509 Corresponding Author

510 *E-mail: kdr@lanl.gov. Phone: 505-667-9457.

511 Notes

512 The authors declare no competing financial interest.

513 ■ ACKNOWLEDGMENTS

514 For financial support of this work, we gratefully acknowledge
515 the support of the U.S. Department of Energy through the
516 LANL/LDRD Program for this work. This work benefited from
517 the use of the time-of-flight neutron reflectometer SPEAR at
518 Lujan Neutron Scattering Center at LANSCE funded by the
519 DOE Office of Basic Energy Sciences and Los Alamos National
520 Laboratory under DOE contract DE-AC52-06NA25396. The
521 authors also gratefully appreciate Dr. Zhong Qun Tian (Xiamen
522 University) for proving SERS particles, Brian Scott (MPA-MC,
523 LANL) for the XRD measurement, and Dr. Mindy Zimmer (C-
524 NR) for the SEM measurements.

■ REFERENCES

- 525
- (1) Morss, L. R.; Edelstein, N. M.; Katz, J. J.; Fuger, J. *The Chemistry of the Actinide and Transactinide Elements*; Springer, 2006. 526
 - (2) Raymond, S.; Bouchet, J.; Lander, G. H.; Le Tacon, M.; Garbarino, G.; Hoesch, M.; Rueff, J. P.; Krisch, M.; Lashley, J. C.; Schulze, R. K.; Albers, R. C. *Phys. Rev. Lett.* **2011**, *107*, 136401. 527
 - (3) He, H.; Shoesmith, D. W. *Phys. Chem. Chem. Phys.* **2010**, *12*, 531
8108. 532
 - (4) Conradson, S. D.; Manara, D.; Wastin, F.; Clark, D. L.; Lander, G. H.; Morales, L. A.; Rebizant, J.; Rondinella, V. V. *Inorg. Chem.* **2004**, *43*, 6922. 533
 - (5) Dubey, M.; Wang, P.; Jablin, M. S.; Mocko, M.; Majewski, J. *Eur. Phys. J. Plus* **2011**, *126*, 7. 536
 - (6) Ashworth, C. D.; Messoloras, S.; Stewart, R. J.; Penfold, J. *Semicond. Sci. Technol.* **1989**, *4*, 1. 538
 - (7) Ashworth, C. D.; Messoloras, S.; Stewart, R. J.; Wilkes, J. G.; Baldwin, I. S.; Penfold, J. *J. Phys. D: Appl. Phys.* **1989**, *22*, 1862. 539
 - (8) Li, J. F.; Huang, Y. F.; Ding, Y.; Yang, Z. L.; Li, S. B.; Zhou, X. S.; Fan, F. R.; Zhang, W.; Zhou, Z. Y.; WuDe, Y.; Ren, B.; Wang, Z. L.; Tian, Z. Q. *Nature* **2010**, *464*, 392. 540
 - (9) Willis, B. T. M. *Nature* **1963**, *197*, 755. 541
 - (10) Hoekstra, H. R.; Siegel, S. J. *Inorg. Nucl. Chem.* **1961**, *18*, 154. 542
 - (11) Loopstra, B. O.; Cordfunke, E. H. P. *Recl. Trav. Chim. Pays-Bas* **1966**, *85*, 135. 543
 - (12) Nowak-Lovato, K. L.; Rector, K. D. *Appl. Spectrosc.* **2009**, *63*, 387. 544
 - (13) Lucas, M.; Macdonald, B. A.; Wagner, G. L.; Joyce, S. A.; Rector, K. D. *ACS Appl. Mater. Interfaces* **2010**, *2*, 2198. 545
 - (14) Armstrong, D. P.; Jarabek, R. J.; Fletcher, W. H. *Appl. Spectrosc.* **1989**, *43*, 461. 546
 - (15) Kips, R.; Pidduck, A. J.; Houlton, M. R.; Leenaers, A.; Mace, J. D.; Marie, O.; Pointurier, F.; Stefaniak, E. A.; Taylor, P. D. P.; Van den Berghe, S.; Van Espen, P.; Van Grieken, R.; Wellum, R. *Spectrochim. Acta, Part B* **2009**, *64*, 199. 547
 - (16) Pointurier, F.; Marie, O. *Spectrochim. Acta, Part B* **2010**, *65*, 797. 548
 - (17) Ruan, C.; Luo, W.; Wang, W.; Gu, B. *Anal. Chim. Acta* **2007**, *605*, 80. 549
 - (18) Leverette, C. L.; Villa-Aleman, E.; Jokela, S.; Zhang, Z.; Liu, Y.; Zhao, Y.; Smith, S. A. *Vib. Spectrosc.* **2009**, *50*, 143. 550
 - (19) Kneipp, K.; Kneipp, H.; Kneipp, J. *Acc. Chem. Res.* **2006**, *39*, 443. 551
 - (20) Fleischmann, M.; Hendra, P. J.; McQuillan, A. J. *Chem. Phys. Lett.* **1974**, *26*, 163. 552
 - (21) Jeanmaire, D. L.; Van Duyne, R. P. *J. Electroanal. Chem.* **1977**, *84*, 1. 553
 - (22) Albrecht, M. G.; Creighton, J. A. *J. Am. Chem. Soc.* **1977**, *99*, 5215. 554
 - (23) Kneipp, K.; Wang, Y.; Kneipp, H.; Itzkan, I.; Dasari, R. R.; Feld, M. S. *Phys. Rev. Lett.* **1996**, *76*, 2444. 555
 - (24) Nie, S.; Emory, S. R. *Science* **1997**, *275*, 1102. 556
 - (25) Kneipp, K.; Kneipp, H.; Itzkan, I.; Dasari, R. R.; Feld, M. S. *Chem. Rev.* **1999**, *99*, 2957. 557
 - (26) Kneipp, K.; Kneipp, H.; Kartha, V. B.; Manoharan, R.; Deinum, G.; Itzkan, I.; Dasari, R. R.; Feld, M. S. *Phys. Rev. E* **1998**, *57*, R6281. 558
 - (27) Halas, N. J.; Lal, S.; Chang, W.-S.; Link, S.; Nordlander, P. *Chem. Rev.* **2011**, *111*, 3913. 559
 - (28) Anema, J. R.; Li, J.-F.; Yang, Z.-L.; Ren, B.; Tian, Z.-Q. *Annu. Rev. Anal. Chem.* **2011**, *4*, 129. 560
 - (29) Fang, Y.; Seong, N.-H.; Dlott, D. D. *Science* **2008**, *321*, 388. 561
 - (30) Parratt, L. G. *Phys. Rev.* **1954**, *95*, 359. 562
 - (31) Siegel, S.; Hoekstra, H. R. *Inorg. Nucl. Chem. Lett.* **1971**, *7*, 455. 563
 - (32) Greaves, C.; Fender, B. E. F. *Acta Crystallogr., Sect. B* **1972**, *28*, 3609. 564
 - (33) He, H.; Andersson, A. D.; Allred, D. D.; Rector, K. D. *Phys. Rev. B* **2012**, submitted for publication. 565
 - (34) Wheeler, V. J.; Dell, R. M.; Wait, E. *J. Inorg. Nucl. Chem.* **1964**, *26*, 1829. 566
 - (35) *Crystal Data. Determinative Tables*; American Crystallographic Association, 1965. 567

- 594 (36) Sato, R. K.; McMillan, P. F. *J. Phys. Chem.* **1987**, *91*, 3494.
595 (37) Palacios, M. L.; Taylor, S. H. *Appl. Spectrosc.* **2000**, *54*, 1372.
596 (38) Rajalakshmi, M.; Arora, A. K. *Nanostruct. Mater.* **1999**, *11*, 399.
597 (39) Stefaniak, E. A.; Alsecz, A.; Sajó, I. E.; Worobiec, A.; Máthé, Z.;
598 Török, S.; Grieken, R. V. *J. Nucl. Mater.* **2008**, *381*, 278.
599 (40) Senanayake, S. D.; Rousseau, R.; Colegrave, D.; Idriss, H. *J.*
600 *Nucl. Mater.* **2005**, *342*, 179.
601 (41) Ackermann, R. J.; Chang, A. T.; Sorrell, C. A. *J. Inorg. Nucl.*
602 *Chem.* **1977**, *39*, 75.
603 (42) Ohwada, K.; Soga, T. *Spectrochim. Acta, Sect. A* **1973**, *29*, 843.
604 (43) Li, W.; Camargo, P. H. C.; Au, L.; Zhang, Q.; Rycenga, M.; Xia,
605 Y. *Angew. Chem., Int. Ed.* **2010**, *49*, 164.